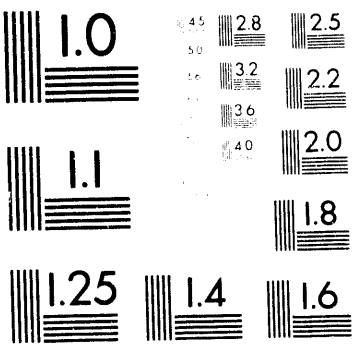
1.0
1.1
1.25
1.4
1.6
1.8
2.0
2.2
2.5
2.8
3.2
3.6
4.0
4.5
5.0

1 of 1

Conf 9310164--3

UCRL-JC-113254
PREPRINT

Analysis of a Proposed Compton Backscatter Imaging Technique

James Hall and Barry Jacoby

This paper was prepared for submittal to
International Symposium
on Substance Identification Technologies
October 4-8, 1993
Innsbruck, Austria

December 1992

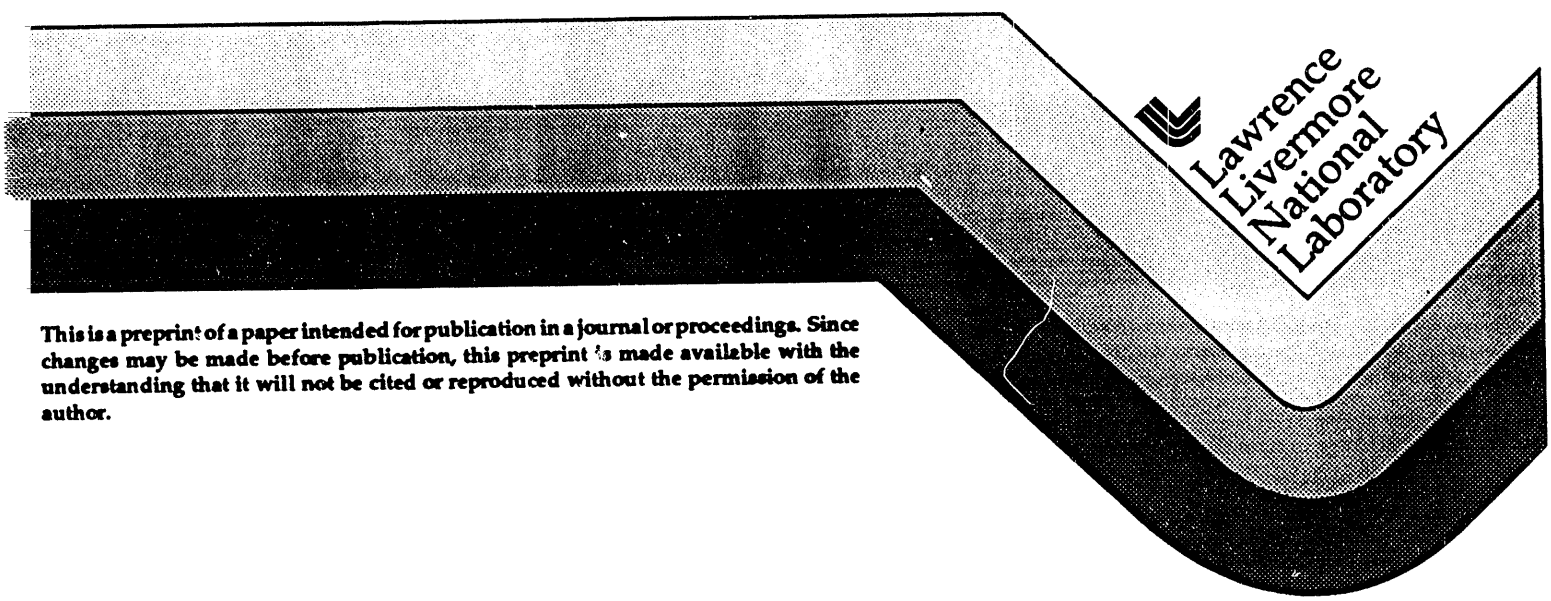

Analysis of a proposed Compton backscatter imaging technique

James Hall and Barry Jacoby

Lawrence Livermore National Laboratory
P.O. Box 808, L-41, Livermore, CA 94551-9900

ABSTRACT

Imaging techniques which require access to only one side of the object being viewed are potentially useful in situations where conventional projection radiography and tomography cannot be applied, such as looking for voids in a large container where access to the back of the object is inconvenient or even impossible. One-sided imaging techniques are currently being used in nondestrucuive evaluation of surfaces and shallow subsurface structures. In this work we present both analytical calculations and detailed Monte Carlo simulations aimed at assessing the capability of a proposed Compton backscatter imaging technique designed to detect and characterize voids located several centimeters below the surface of a solid. The proposed technique, based on a scheme suggested by Farmer and Collins[2], encodes the spatial position and structure of voids in a solid in the energy spectrum of the Compton-scattered photons as recorded by a high resolution detector. Our calculations model a ^{137}Cs source projecting a 1 mm^2 pencil beam of 662 keV gammas into a target slab at an incident angle of 45° and a collimated detector (also oriented at 45° with respect to the surface) which views the beam path at a central angle of 90°. The detector collimator is modeled here as a triangular slit viewing a 2.54 cm (1.000") segment of the beam path at a depth of 2 cm below the surface of the slab. Our results suggest that the proposed technique should be capable of an absolute position resolution of ≈ 0.25 mm (≈ 0.010") for isolated voids and an overall object resolution of ≈ 1.00 lp/mm (≈ 0.040"). The predicted signal contrast for voids packed with various contraband materials (e.g. Semtex, cocaine-HCl, etc.) will be discussed as well as multiple scattering contributions to the predicted yields.

1. INTRODUCTION

Projection radiography is the predominant technique currently used in nondestructive testing (NDT) of materials. In projection radiography, x rays or gamma rays transmitted through the object under inspection are used for imaging purposes; however, for photon energies in the range of ≈ 100 keV to 10 MeV, incoherent Compton scattering dominates the interaction process and actually represents a larger fraction of the overall energy expended in the imaging process. Imaging techniques based on the detection and analysis of this scattered radiation may therefore provide important, complimentary, inspection opportunities for those involved in NDT.

Backscatter imaging techniques offer several important advantages over conventional transmission radiography. Forward scattering techniques typically require unrestricted access to both sides of the object being viewed, while backscatter techniques allow for one-sided inspection geometries. Systems requiring access to only one side of the object under inspection are potentially useful in situations where conventional radiography and reconstructive tomography cannot be easily applied, such as searching for voids in a wall or container where access to the back of the object is convenient or even impossible. Backscatter imaging techniques also allow for simple, direct 3-dimensional imaging with true depth information without the need for mathematical reconstruction.

A number of efforts have been made to apply backscatter imaging in medical and industrial areas. In the medical field, P. G. Lale first began investigating the use of backscattered radiation in the x-ray imaging of human internal tissues as early as 1959.[1] F. T. Farmer and M. P. Collins later applied Compton imaging to the determination of anatomical cross sections of the human body.[2,3] In the late 1970's, J. J. Battista and M. J. Bronskill developed techniques for measuring the electron density of human tissue using backscattered radiation.[4] In the industrial field, D. G. Costello, *et al.* have used Compton imaging to develop an automated system for remotely examining artillery shells[5] and J. Kosanetzky, *et al.* have adapted an apparatus designed for medical imaging ("ComScan") to image shallow subsurface structures in light metal alloys, laminates and plastics.[6] R. H. Bossi, *et al.* of Boeing Aerospace have also applied Compton imaging techniques to evaluate aluminum and plastic structures[7] using an innovative "flying spot" x-ray backscatter imaging system developed by American Science and Engineering.[8] R. Guzzardi and G. Licitra have recently published a critical review of Compton imaging which outlines the current state of the art and provides an excellent general reference on the subject including many addition examples of its use in medicine and industry.[9]

We have recently undertaken the analysis of a Compton backscatter imaging technique proposed by one of us (BJ) for use in industrial NDT. Based on the scheme suggested by Farmer and Collins, the proposed technique would be used to detect and characterize voids located several centimeters below the surface of a solid. In this work, we present analytical and Monte Carlo calculations aimed at assessing the ultimate capabilities of the proposed technique. Our calculations include predicted Compton-scattered photon spectra for iron and wood targets with various embedded voids, estimates for detected yields, limits on position and object resolution, and sensitivity to target density fluctuations. Background contributions due to multiple scattering are also discussed.

2. COMPTON SCATTERING THEORY

Compton scattering theory describes the inelastic scattering of photons by loosely bound target electrons, in which a part of the initial photon energy is lost to the recoil electron (the electron is considered to be loosely bound if its binding energy is small compared to the incident photon energy). The energy of the scattered photon is given by:

$$E' = \frac{E}{(1+\gamma(1-\cos(\theta)))}, \qquad \gamma = \frac{E}{m_o c^2}, \tag{1}$$

where E is the incident photon energy, θ is the scattering angle, and m_o is the rest mass of the electron. The angular distribution of Compton-scattered photons is given by the differential cross section per unit solid angle for the collision. This cross section is given by the familiar Klein-Nishina formula:[10]

$$\frac{d\sigma(E,\cos(\theta))}{d\Omega} = r_o^2 \frac{(1+\cos^2(\theta))}{2} \left\{ \frac{1}{(1+\gamma(1-\cos(\theta)))^2} \times \left\{ 1 + \frac{\gamma^2(1-\cos(\theta))^2}{(1+\cos^2(\theta))(1+\gamma(1-\cos(\theta)))} \right\} \right\}, \tag{2}$$

where r_o is the classical radius of the electron. The angular dependence of this expression is illustrated in Figure 1 for incident photon energies of 0.100 MeV and 0.662 MeV (typical of x-ray and gamma-ray backscatter imaging schemes). The scattering cross section is observed to peak at forward angles ($\approx 0°$) and tends to fall off rapidly in both cases as one moves toward 90° scattering. The cross section rises slightly at larger scattering angles for 0.100 MeV x-rays, but remains relatively flat above $\approx 100°$ for 0.662 MeV gammas.

3. PROPOSED IMAGING TECHNIQUE

Several approaches to Compton backscatter imaging have been suggested in the literature. The original idea developed by Lale[1] examined the target point-by-point by using Soller-like pinhole collimators to focus the detector view angle to the scattering point of interest. This method requires a large number of individual measurements (with either the source or detector being moved each time) in order to scan the full target volume. The approach suggested by Farmer and Collins[2,3] uses a detector with a triangular slit collimator to obtain line scans of the target, thereby greatly reducing the overall imaging time. The radiation scattered into the detector from each point along a line scan has a characteristic energy E' which is a unique function of the scattering angle θ (*cf.* Eq. 1) and therefore of distance along the beam path. Spatial position is thus encoded in the energy spectrum recorded by the detector.

The imaging technique under consideration in this work is based on the scheme of Farmer and Collins. The basic geometry modeled in our calculations is illustrated in Figure 2. A "pencil" beam (1 mm^2 cross section) of 0.662 MeV gamma rays from a ^{137}Cs source is projected into the target slab at an angle of 45° with respect to the surface. A collimated detector (also oriented at 45° with respect to the surface) views the beam path within the solid at a central angle of 90°. The collimator is modeled as a 1 mm thick triangular slit with a penumbra (denoted by dashed lines) which encloses a 2.54 cm segment of the beam path centered (in most cases considered) at a depth of 2 cm below the surface of the slab. The detector aperture is set at a width of 0.254 mm (this has the effect of limiting the ultimate energy resolution in our model to $\approx \pm 0.150$ keV). The detector face is positioned ≈ 7 cm above the slab, providing a direct line of sight to the surface of ≈ 10 cm.

4. ANALYTICAL CALCULATIONS

Single-scattered photons are of primary interest in most Compton imaging schemes since, as noted above, the energies of

these photons can be directly correlated to spatial positions within the target. For a monoenergetic source, an analytical estimate for the detected yield of single-scattered photons may be obtained by integrating over the beam volume within the collimator penumbra (*cf.* Fig. 2) according to

$$Y_1 = \int_{V_1} I_0 \, e^{-r_{01}/\lambda_0} \, n_e \, \frac{d\sigma(\cos(\theta_1))}{d\Omega} \, \frac{e^{-r'_{12}/\lambda_1}}{r_{12}^2} \cos(\eta) \, dA_2 \, dV_1 \,, \tag{3}$$

where

I_o = incident beam intensity (# / cm^2 - sec) ,

r_{01} = path length 0 $\rightarrow$ 1 (cm) (*cf.* Fig. 2) ,

λ_o = photon mean free path at incident beam energy (cm) ,

n_e = target electron density (e^- / cc) ,

$\frac{d\sigma(\cos(\theta_1))}{d\Omega}$ = differential scattering cross section (cm^2 / e^- - sr) ,

$\cos(\theta_1) = \hat{r}_{01} \cdot \hat{r}_{12} = \sin(\alpha)\frac{(x_2 - x_1)}{r_{12}} - \cos(\alpha)\frac{(z_2 - z_1)}{r_{12}}$,

r_{12} = path length 1 $\rightarrow$ 2 (cm) (*cf.* Fig. 2) ,

r'_{12} = path length 1 $\rightarrow$ surface (cm) $= -\frac{r_{12} z_1}{(z_2 - z_1)}$,

λ_1 = photon mean free path at scattered energy (cm) ,

$\cos(\eta)$ = cosine of angle between $\bar{r}_{12}$ and detector normal

$= \sin(\beta)\frac{(x_2 - x_1)}{r_{12}} + \cos(\beta)\frac{(z_2 - z_1)}{r_{12}}$,

dA_2 = area of detector aperature (cm^2) ,

dV_1 = beam volume within collimator penumbra (cm^3) .

Given the present problem, and assuming (for example) an iron target slab with electron density ≈ 2.20E+24 e^-/cc, numerical evaluation of Equation 3 predicts a detected yield of ≈ 2.85E-08 counts per second per photon in the incident beam. For reasonably attainable laboratory beam intensities of ≈ 9.00E+06 γ/cm^2-sec, this works out to ≈ 0.25 counts per second.

In addition to the yield of single-scattered photons, the detector will also record an unwanted background contribution due to multiply-scattered photons. These multiply-scattered photons interact first along the incident beam path and then undergo at least one subsequent interaction within the collimator penumbra before reaching the detector. An estimate for the yield of double-scattered photons may be obtained by extending Eq. 3 to give

$$Y_2 = \int_{V_1}\int_{V_2} I_0 \, e^{-r_{01}/\lambda_0} \, n_e \, \frac{d\sigma(\cos(\theta_1))}{d\Omega} \, \frac{e^{-r_{12}/\lambda_1}}{r_{12}^2} \times n_e \, \frac{d\sigma(\cos(\theta_2))}{d\Omega} \, \frac{e^{-r'_{23}/\lambda_2}}{r_{23}^2} \cos(\eta) \, dA_3 \, dV_2 \, dV_1 \tag{4}$$

where the detector aperture is now taken to be point "3" (*cf.* Fig. 2) and point "2" is an arbitrary point within the collimator penumbra. In spite of its similarity to Eq. 3, Equation 4 is impractical (if not altogether impossible) to evaluate accurately. The problem lies in integrating the first attenuation / solid angle factor (between points 1 and 2) over the collimator penumbra. While this factor could be easily integrated using spherical coordinates, it is impossible to formulate suitably general limits of integration over the penumbral volume in this system. If the penumbra is represented using Cartesian coordinates instead, the factor produces a roving singularity and most numerical integration techniques fail to converge.

5. MONTE CARLO SIMULATIONS

In addition to our analytical calculations, we have also carried out a series of Monte Carlo simulations of the proposed imaging technique using a detailed neutron and gamma-ray transport code ("COG") originally developed by LLNL for use in the nuclear test program.[11] The COG formalism is versatile enough to allow us to model radiation sources, 3-dimensional system geometries, elemental distributions, and detector arrays to virtually any level of accuracy required. The simulations presented here were carried out on Lawrence Livermore's Y/MP CRAY computer, with each run requiring ≈ 100 minutes of CPU time. Each run, simulating the problem outlined in Section 3, tracked 100,000 incident gammas through the full system geometry, resulting in typical statistical deviations of 2 - 3% over the spectral range of interest.

Our initial COG simulations were aimed at predicting energy spectra for Compton-scattered photons and estimating the detected yields and background contributions due to multiple scattering for several baseline problems involving 0.662 MeV gammas incident on iron and wood target slabs both with and without embedded voids. In each run, the detector collimator was aimed at a point 2 cm below the surface of the slab (*cf.* Fig. 2). Typical spectra for iron and wood slabs (without embedded voids) are presented in Figures 3a and 3b, respectively. The rectangular peaks near 0.290 MeV correspond to the energy range accepted by the detector collimator (≈ 0.272 MeV - 0.306 MeV). The much higher attenuation of gammas in the incident beam for the case of iron compared to wood results in an enhancement of forward-angle (< 90°), high-energy (> 0.300 MeV) scattering at points along the incident beam path just inside the iron slab. This accounts for the relatively larger high energy background observed in the iron spectrum.

The energy range accepted by the detector collimator is shown in more detail in Figures 4a - 4d. The baseline spectrum for an iron target with no voids (Fig. 4a) has a steep positive slope over the range of interest, due primarily to our particular beam-collimator geometry and high attenuation within the target. Scattered photons from points lying just inside the collimator penumbra have a relatively higher energy (and hence lower attenuation) than those coming from points near the far end of the penumbra (*cf.* Fig. 2). Due to the scattering geometry, these photons also have a shorter path length to traverse in exiting the slab. These two factors combine to produce the slope observed in Figure 4a (the scattering cross section is essentially constant over the range of angles involved (*cf.* Fig. 1)). The COG simulation predicts a detected yield of ≈ 5.10E-08 counts per second per photon in the incident beam with a multiple-scattering contribution of ≈ 40% (this works out to a single-scattered photon yield of ≈ 3.06E-08 counts per second per photon in the incident beam, which agrees well with our analytical estimate of ≈ 2.85E-08). Comparing the COG spectrum (which includes all orders of scattering) with a predicted spectrum for single-scattered photons obtained during evaluation of Equation 3, it appears that multiple scattering contributes very little to the signal at high energies, but increases in importance as one moves toward lower scattering energies.

The predicted spectrum for the case of scattering from an iron target slab with a small void embedded 2 cm below the surface is shown in Figure 4b. The void was modeled here as a structureless cube, 2 mm on a side, oriented normal to the incident beam. The void produces a well defined gap of width ≈ 2.5 keV in the COG spectrum at a central energy of ≈ 0.288 MeV. If we define the contrast at a given energy E as

$$C = \left| \frac{\text{Response } (E) \text{ (no voids)} - \text{Response } (E) \text{ (void)}}{\text{Response } (E) \text{ (no voids)}} \right|, \tag{5}$$

then the contrast at the void position is seen to be ≈ 85%. Given the dimensions of the void compared to those of the incident beam, the contrast at this position could be expected to be ≈ 100% if single scattering was the only contribution to the detected yield. The observed contrast of ≈ 85% is consistent with a multiple-scattering contribution of ≈ 15% at the void position obtained by comparing the COG simulation with our analytical calculation (*cf.* Fig. 4a).

The baseline spectrum for a wood target slab with no voids is shown in Figure 4c. In contrast to the iron target, the predicted spectrum for wood (electron density ≈ 2.45E+23 e⁻/cc) is relatively flat over the range of interest. This is the result of a much lower attenuation of incident and scattered gammas in wood than in iron. The COG simulation predicts a detected yield of ≈ 8.56E-08 counts per second per photon in the incident beam with a multiple-scattering contribution of ≈ 5% (this works out to a single-scattered yield of ≈ 8.13E-08, which again agrees well with our analytical estimate of ≈ 8.03E-08 for this case). The predicted spectrum for single-scattered photons obtained during evaluation of Equation 3 is virtually coincident with the COG simulation over the range of interest, which implies that multiple scattering is relatively insignificant for wood targets. This is not really surprising since, as can be seen from Equation 4, double scattering (the primary component of multiple scattering) is proportional to the square of the electron density and thus falls off rapidly as one moves toward lower Z targets. What *is* surprising, however, is that the predicted yield for the wood target is actually higher than for the iron target. This implies that the larger scattering cross section in iron compared to wood is apparently more than outweighed by

the lower absorption of incident and scattered gammas in wood compared to iron.

The predicted spectrum for the case of scattering from a wood target with a small void embedded 2 cm below the surface is shown in Figure 4d. The void was again modeled as a 2 mm cube oriented normal to the incident beam. The void produces a well defined gap in the COG spectrum with a contrast of ≈ 95% at the centroid position. The observed contrast is consistent with the multiple-scattering contribution of ≈ 5% predicted by COG.

An estimate for the absolute position resolution of the proposed imaging technique (*i.e.* it's ability to resolve different depths or changes in position) was obtained by running a series of simulations in which void positions were varied by some small amount between runs. Figure 5a shows the COG spectra for iron targets with voids which have been shifted by 0.254 mm (0.010") with respect to one another (the voids are the same simple, 2 mm cubes located 2 cm below the surface as before). The shift in gap position between runs is easily seen. Figure 5b shows an expanded view of the energy region of interest with the COG spectrum convolved with a 1 keV (FWHM) Gaussian (representing the highest energy resolution that one could likely find in commercially available gamma detectors). The centroids of the gaps are separated by ≈ 0.3 keV, which should be resolvable in actual experiments.

An estimate for the absolute object resolution of the proposed technique (*i.e.* it's ability to resolve two closely spaced objects) was obtained by running a series of simulations in which structured voids were used to mock up line resolution charts of various optical densities. The voids were modeled as 2 mm X 2 mm X 1 cm rectangles containing grid structures simulating resolutions of 0.5 lp/mm to 2.0 lp/mm and centered at a depth of 2 cm below the surface of the target slab. An analysis of the results is presented in Figures 6a - 6d. The COG spectrum for the case of an iron target with a 0.50 lp/mm structured void (corresponding to an object resolution of 2.000 mm (0.079")) is shown in Figure 6a. The structure is clearly visible in this spectrum. Figure 6b shows an expanded view of the energy region of interest with the COG spectrum convolved with a 1 keV (FWHM) Gaussian. The structure is still clearly visible in the convolved spectrum, with an estimated contrast of ≈ 73%, implying that objects separated by ≈ 2 mm should be easily resolved in actual experiments. Figure 6c shows the same analysis as Figure 6b for the case of a 1.00 lp/mm structure (corresponding to a resolution of 1.000 mm (0.039")). The estimated contrast drops to ≈ 21%, but the grid structure is still visible in the convolved spectrum, implying that objects separated by ≈ 1 mm should also be resolvable in practice. Finally, Figure 6d presents the analysis for a 1.50 lp/mm grid (corresponding to a resolution of 0.667 mm (0.026")). The grid structure is no longer resolved in the convolved spectrum, implying that objects separated by less than ≈ 0.75 mm will probably not be resolved in practice. This limit is consistent with a simple hand calculation which indicates that a distance of 0.794 mm (0.031") along the beam path corresponds to an energy difference of ≈ 1 keV at the detector.

Changes in detected yield and signal contrast with increasing void depth were investigated by moving a structureless 2 mm cubical void along the beam path to various depths (the detector was also repositioned to keep the void centered in the collimator penumbra). The COG spectra for iron targets with voids at depths of 2 and 4 cm are shown in Figure 7a. The predicted yield is observed to decrease by a factor of ≈ 35 going from 2 to 4 cm, while the multiple-scattering contribution increases from ≈ 40% to ≈ 65%. Surprisingly, the signal contrast at the void position remains relatively constant at ≈ 85%. However, given the precipitous drop in predicted yield and the rise in multiple scattering as one moves toward greater void depths, it would appear that the proposed technique (using a 0.662 MeV gamma source) is probably not suited for imaging depths greater than ≈ 2 - 3 cm in high-Z targets such as iron.

The COG spectra for wood targets with 2 mm cubical voids at depths of 2, 4, and 8 cm are shown in Figure 7b. The predicted yield in this case decreases by less than a factor of two in going from a depth of 2 to 4 cm and by only a factor of ≈ 6 between 2 and 8 cm. Multiple scattering increases only slightly over this range, going from ≈ 5% at 2 cm to ≈ 10% at 8 cm. The contrast at the void position again remains relatively constant at ≈ 95%. These results imply that the proposed technique should be useful for detecting and imaging voids at depths of up to ≈ 8 - 10 cm in low-Z targets such as wood.

Finally, the sensitivity of the proposed technique to density fluctuations in iron and wood targets was investigated by filling a 2 mm cubical void located 2 cm below the surface with materials of various densities. The predicted spectrum for an iron target in which the void has been filled with iron at 90% of nominal density is shown in Figure 8a. The inclusion is barely visible in this case, even with reasonably good counting statistics (estimated at ≈ 3%). Figure 8b shows the case for an iron target in which the void has been filled with iron at 80% of nominal density. The inclusion is now visible, but still not really defined well enough to image reliably. One problem of potential interest suggested during the course of these calculations is shown in Figure 8c, in which the void in the iron target has been packed with cocaine-HCl at a typical shipping density of 0.90 g/cc (n_e ≈ 2.87E+23 e⁻/cc). The inclusion is clearly visible in the predicted spectrum, with a contrast of ≈ 65% at the centroid position. For the case of a wood target (Fig. 8d), the cocaine-HCl inclusion is just detectable above the back-

ground, with a contrast of ≈ 15%. Based on these results, it would appear that the technique should be sensitive to target density fluctuations of ≈ 10% - 15%, even at relatively large depths.

6. CONCLUSIONS

The purpose of this study was to assess the capabilities of the imaging technique proposed in Section 3 using analytical calculations and Monte Carlo simulations prior to carrying out actual experiments. It is apparent from the results presented here that the performance of this (or any other) backscatter imaging system will depend on several factors. The signal contrast at the position of a void or inclusion in a solid target will be limited by counting statistics, multiple scattering, density differentials, and the relative size and shape of the incident beam compared to the void or inclusion. The ultimate resolution of the technique will be limited by the energy resolution of the detector, the diameter of the incident beam, and the size of the detector aperture. Unfortunately, designs which maximize the signal contrast may do so at the expense of image resolution and visa versa. Compromises in design therefore usually must be made.

The imaging technique considered in the present work was designed for applications requiring high spatial resolution. The detector was therefore modeled as having an energy resolution of ≈ 1 keV at ≈ 0.300 MeV ($\Delta E/E \approx 0.33\%$). While this represents an admittedly optimistic value for energy resolution, it is certainly not an unrealistic goal. The incident beam was modeled as a "pencil" beam of cross section 1 mm X 1 mm. Although true "pencil" beams cannot be made in practice, it should be possible to collimate the incident beam so that it has a diameter of ≈ 1 mm at any given depth in the target. Finally, the detector aperture was modeled here as having a width of only 0.254 mm. While this supports high spatial resolution, it also greatly reduces the predicted yield at the detector. Based on the results of this study, it appears that the detector aperture could be opened up to a width of ≈ 1 mm without significantly affecting the resolution of the technique. This would increase the predicted yield by a factor of four, thus making target density measurements much easier.

The proposed Compton imaging technique appears promising for some applications, given a detector with sufficiently high energy resolution. The technique promises high spatial resolution with relatively low backgrounds due multiple scattering (particularly in low-Z targets) and should be capable of detecting and characterizing voids several centimeters below the surface of a solid. The predicted yields are relatively low for this scheme compared to some "open-collimator" designs, but it might still be competitive if background noise levels can be kept below ≈ 0.02 cps.

7. ACKNOWLEDGMENTS

This work was performed at the University of California, Lawrence Livermore National Laboratory under the auspices of the U.S Department of Energy (contract # W-7405-Eng-48).

8. REFERENCES

[1] P. Lale, "The Examination of Internal Tissues, using Gamma-ray Scatter with a possible Extension to Megavoltage Radiography," *Phys. Med. Biol.*, **4**, 159 (1959).

[2] F. Farmer and M. Collins, "A New Approach to the Determination of Anatomical Cross-sections of the Body by Compton Scattering of Gamma-Rays," *Phys. Med. Biol.*, **16**, 577 (1971).

[3] F. Farmer and M. Collins, "A Further Appraisal of the Compton Scattering Method for Determining Anatomical Cross-sections of the Body," *Phys. Med. Biol.*, **19**, 808 (1974).

[4] J. Battista and M. Bronskill, "Compton-scatter Tissue Densitometry: Calculation of Single and Multiple Scatter Photon Fluences," *Phys. Med. Biol.*, **23**, 1 (1978).

[5] D. Costello, J. Stokes, and A. Trippe, "Theory and Applications of Collimated Photon Scattering," *14th Symposium on Nondestructive Evaluation*, San Antonio, TX (1971).

[6] J. Kosanetzky, G. Harding, K. Fischer, and A. Meyer, "Compton backscatter tomography of low atomic number materials with the ComScan system," Philips GmbH (private communication).

[7] R. Bossi, K. Friddell, and J. Nelson, "Backscatter X-Ray Imaging," *Mat. Eval.*, 46, 1462 (1988).

[8] For additional information, contact: American Science and Engineering, Cambridge, MA 02139, (617) 868-1600.

[9] R. Guzzardi and G. Licitra, "A Critical Review of Compton Imaging," *CRC Crit. Rev. Bio. Eng.*, 15, 237 (1988).

[10] R. Evans, *The Atomic Nucleus* (McGraw-Hill, New York, 1955), pp. 677 - 693.

[11] T. Wilcox and E. Lent, *COG - A Particle Transport Code Designed to Solve the Boltzman Equation for Deep-Penetration (Shielding) Problems, Vol. 1 Users Manual*, LLNL Rept. # M-221-1 (1989).

9. COLLECTED FIGURES

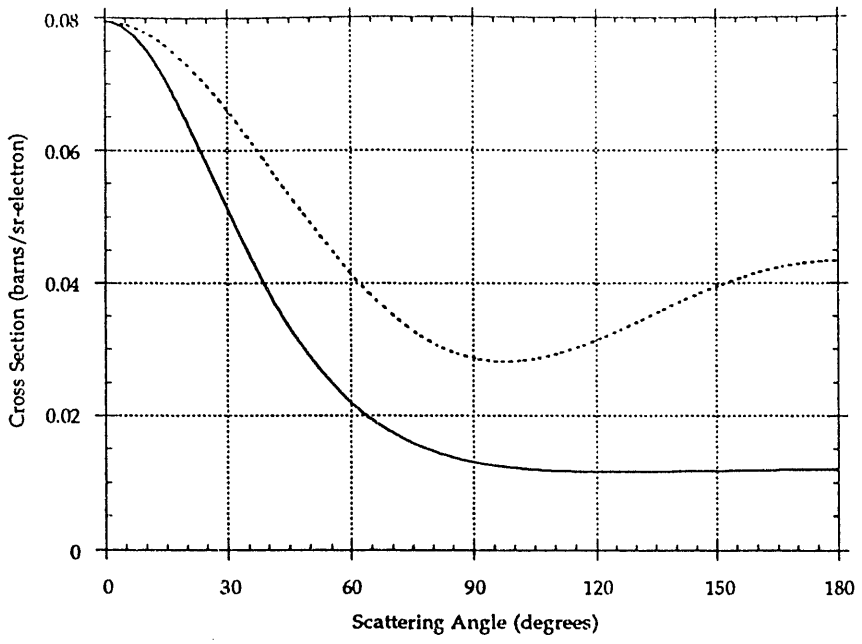

Figure 1 - Angular dependence of the Klein-Nishina formula for the differential Compton-scattering cross section for incident photon energies of 0.662 MeV (solid line) and 0.100 MeV (dashed line).

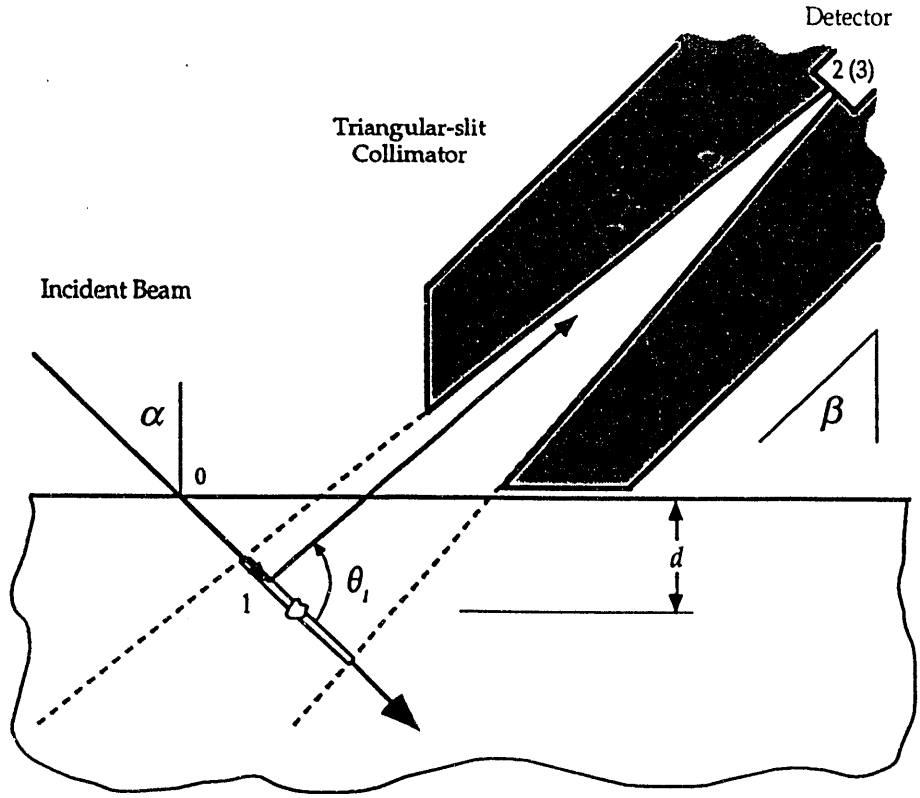

Figure 2 - Generalized geometrical layout of proposed Compton backscatter imaging technique.

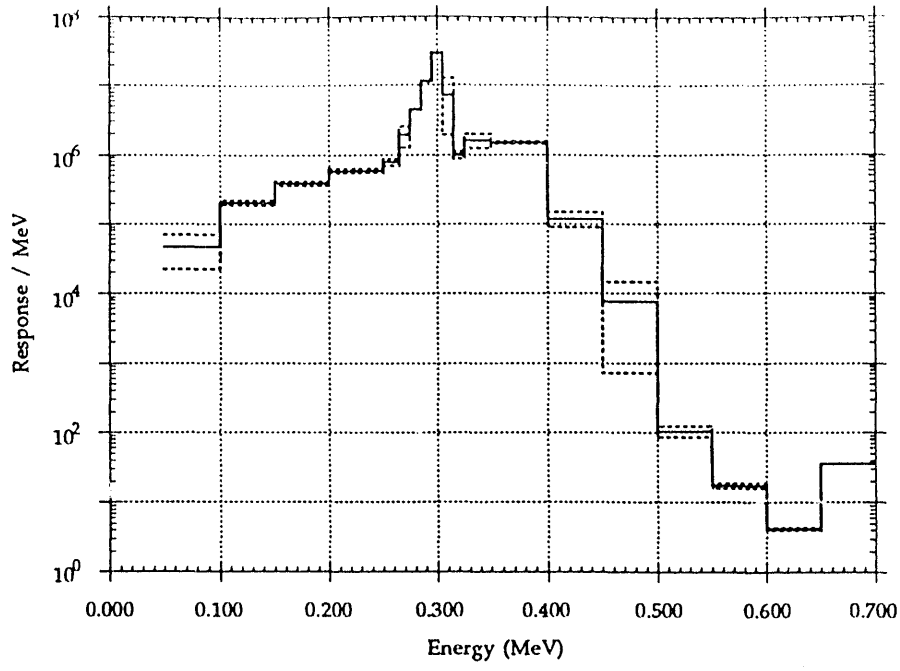

Figure 3a - Typical COG spectrum for an iron target slab (error bars represent ± 1 σ); detector collimator was aimed at a point 2 cm below the surface of the slab.

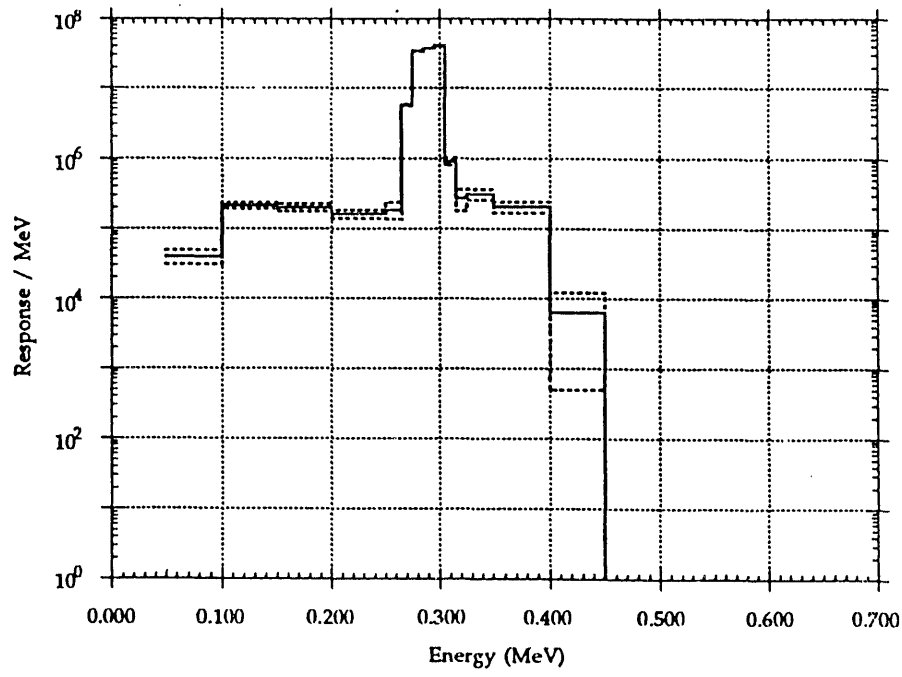

Figure 3b - Typical COG spectrum for a wood target slab (error bars represent ± 1 σ); detector collimator was aimed at a point 2 cm below the surface of the slab.

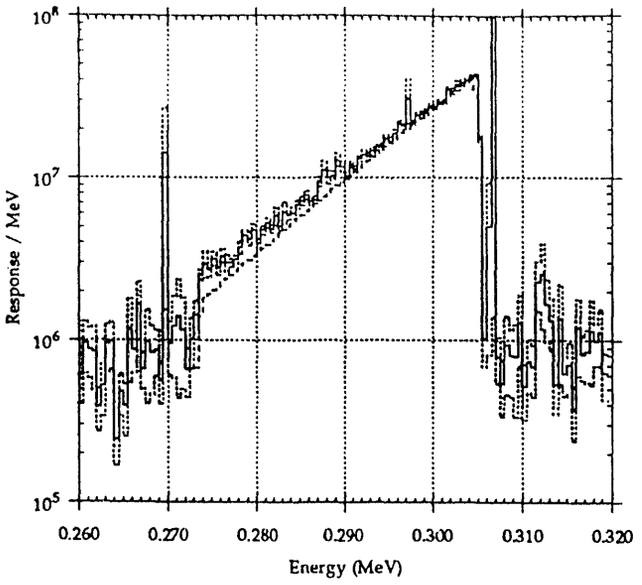

Figure 4a - COG spectrum for an iron target with no voids (solid line) compared to an analytical calculation (heavy dashed line) (error bars represent ± 1 σ).

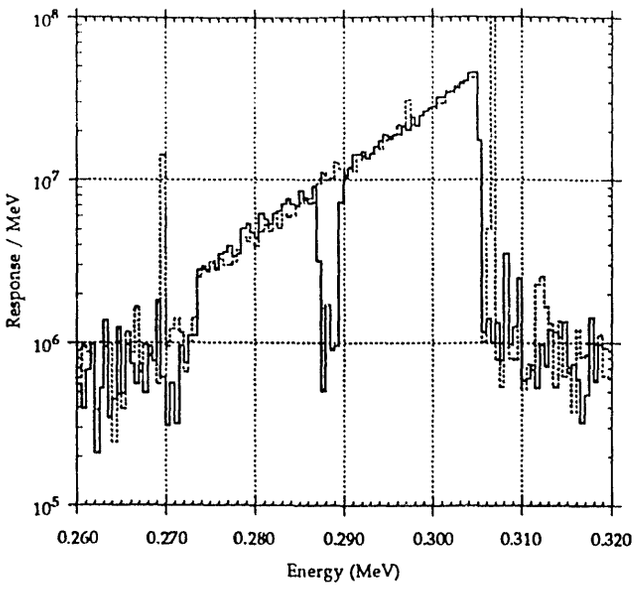

Figure 4b - COG spectrum for an iron target with a 2 mm cubical void 2 cm below the surface (solid line) compared to the baseline iron spectrum with no voids (dashed line) (*cf.* Fig. 4a)).

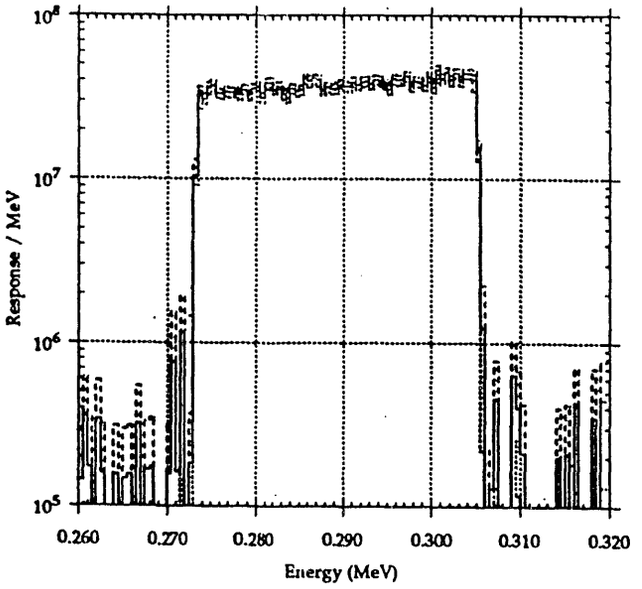

Figure 4c - COG spectrum for a wood target with no voids (solid line) compared to an analytical calcuation (heavy dashed line) (error bars represent ± 1 σ).

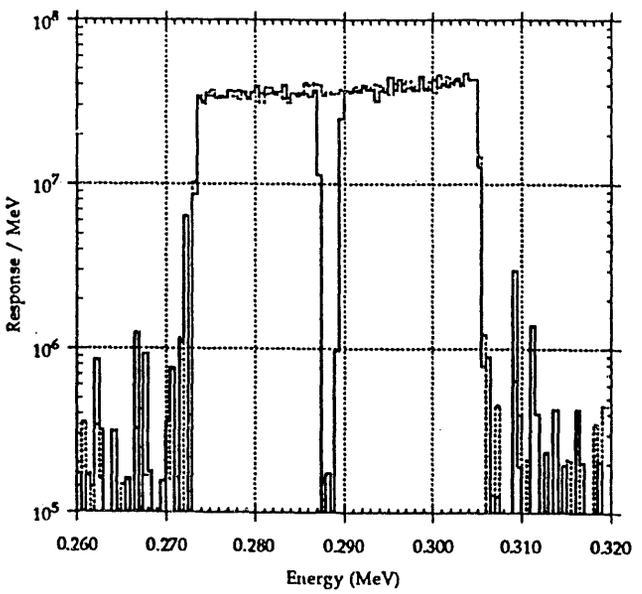

Figure 4d - COG spectrum for a wood target with a 2 mm cubical void 2 cm below the surface (solid line) compared to the baseline wood spectrum with no voids (dashed line) (*cf.* Fig. 4c)).

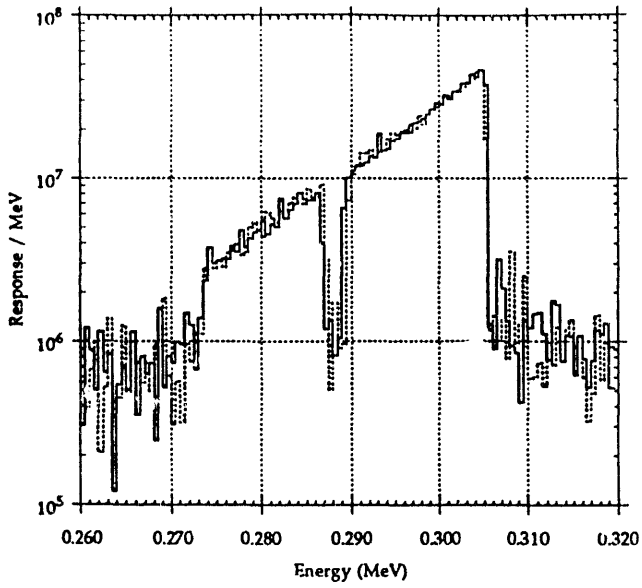

Figure 5a - COG spectra for iron targets with 2 mm cubical voids separated by 0.254 mm (0.010").

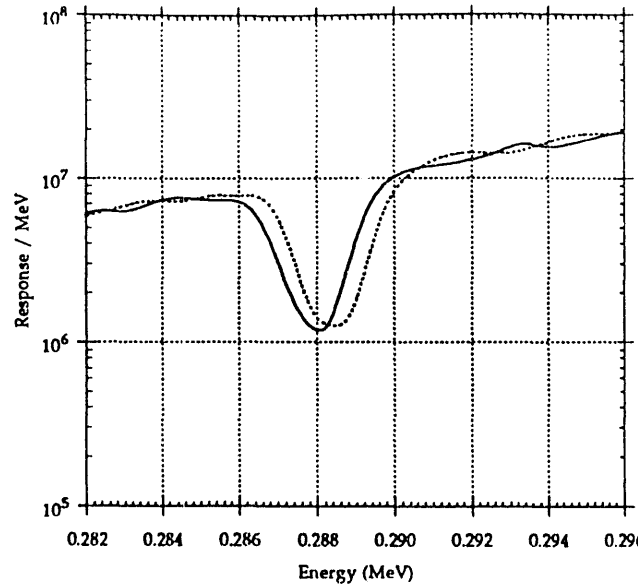

Figure 5b - Expanded view of previous COG spectra convolved with a 1 keV (FWHM) Gaussian resolution function.

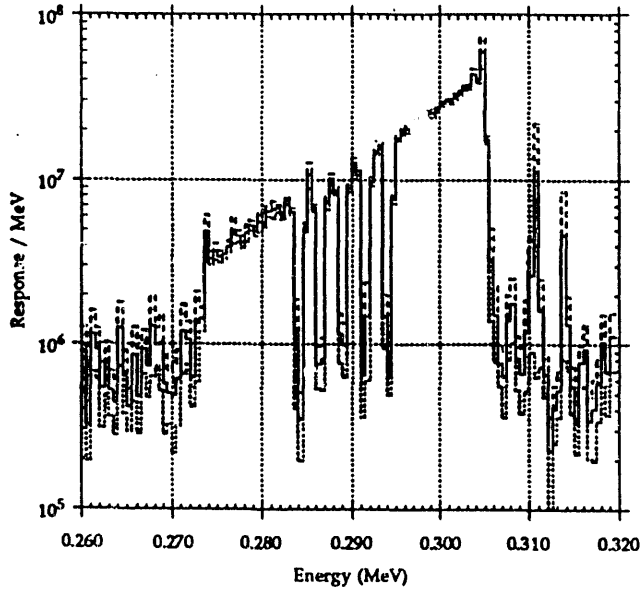

Figure 6a - COG spectrum for an iron target with a structured void representing an object resolution of 0.5 lp/mm (error bars represent ± 1 σ).

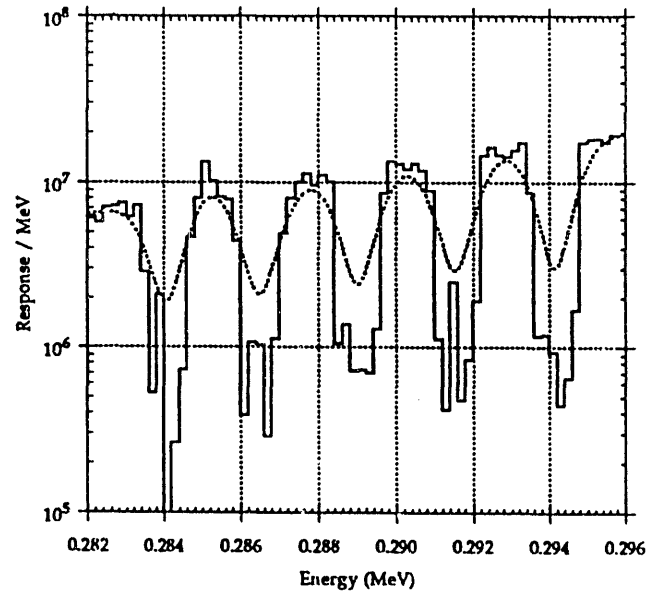

Figure 6b - Expanded view of previous COG spectrum (solid line) convolved with a 1 keV (FWHM) Gaussian resolution function (dashed line).

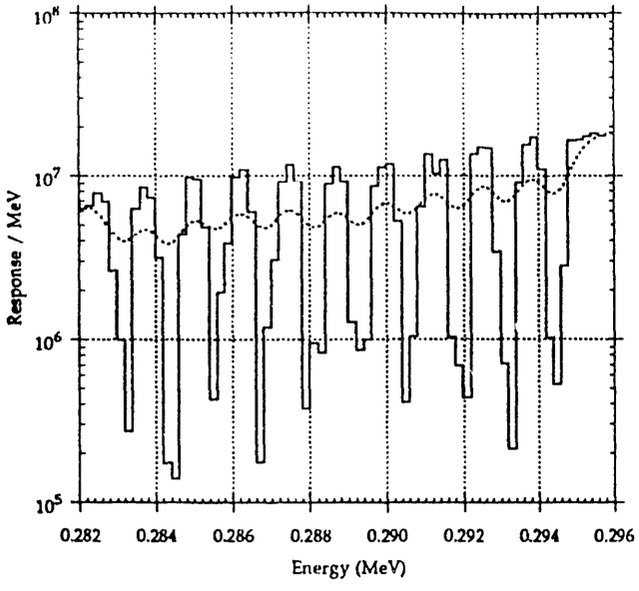

Figure 6c - Expanded view of COG spectrum for an iron target with a structured void representing an object resolution of 1.0 lp/mm (solid line), convolved with a 1 keV (FWHM) Gaussian resolution function (dashed line).

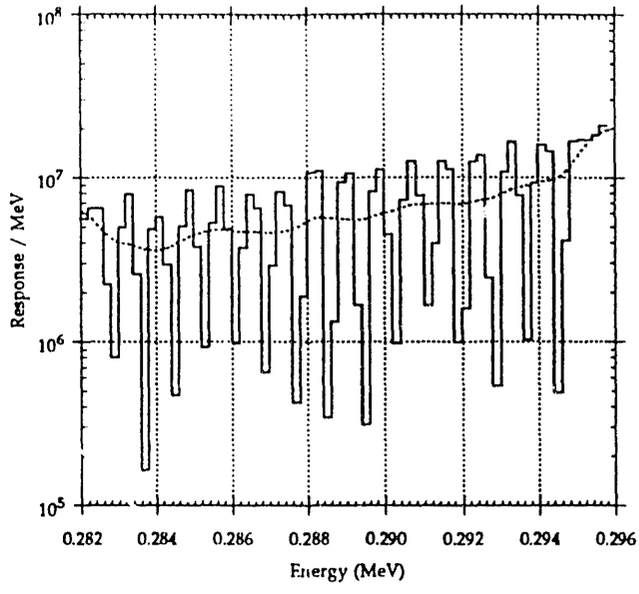

Figure 6d - Expanded view of COG spectrum for an iron target with a structured void representing an object resolution of 1.5 lp/mm (solid line) convolved with a 1 keV (FWHM) Gaussian resolution function (dashed line).

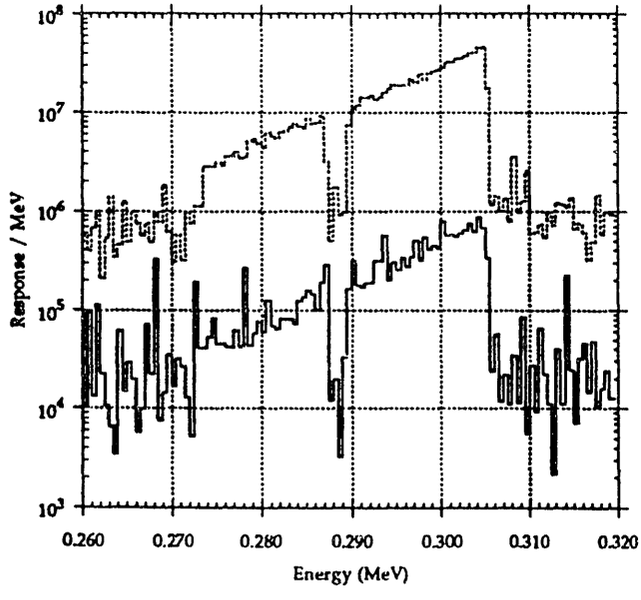

Figure 7a - COG spectra for iron targets with 2 mm cubical voids embedded at depths of 2 cm (dashed line) and 4 cm (solid line) below the surface.

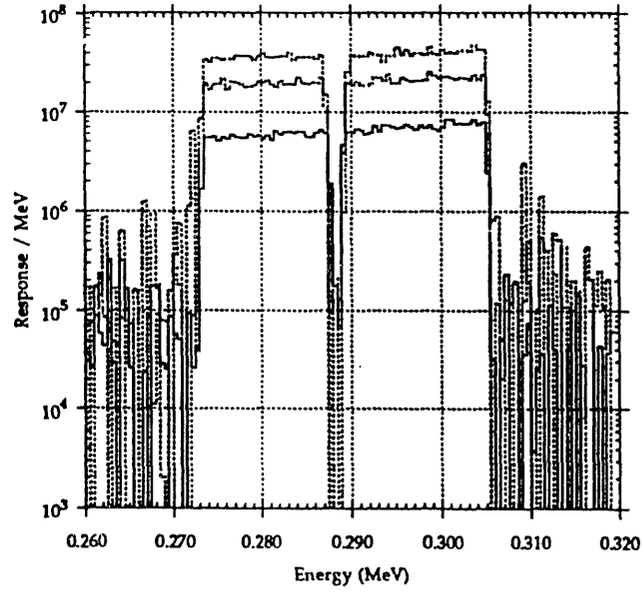

Figure 7b - COG spectra for wood targets with 2 mm cubical voids embedded at depths of 2 cm, 4 cm (dashed lines), and 8 cm (solid line) below the surface.

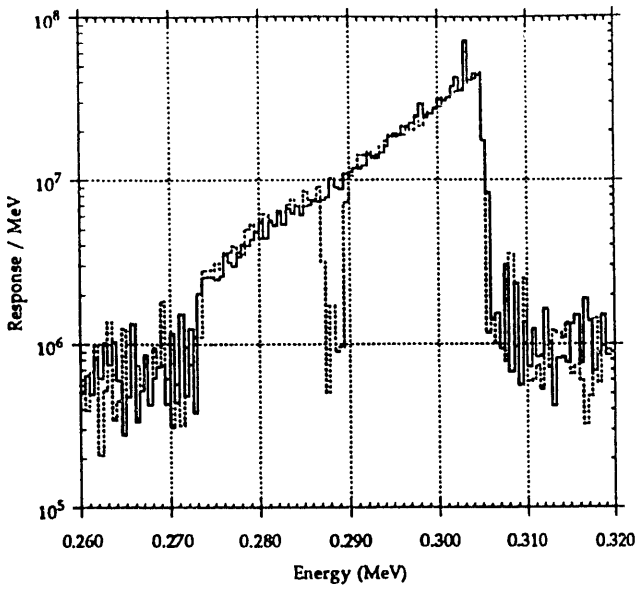

Figure 8a - COG spectrum for an iron target with a 2 mm void filled with iron at 90% nominal density (solid line) compared to the baseline iron spectrum with an air-filled void (dashed line).

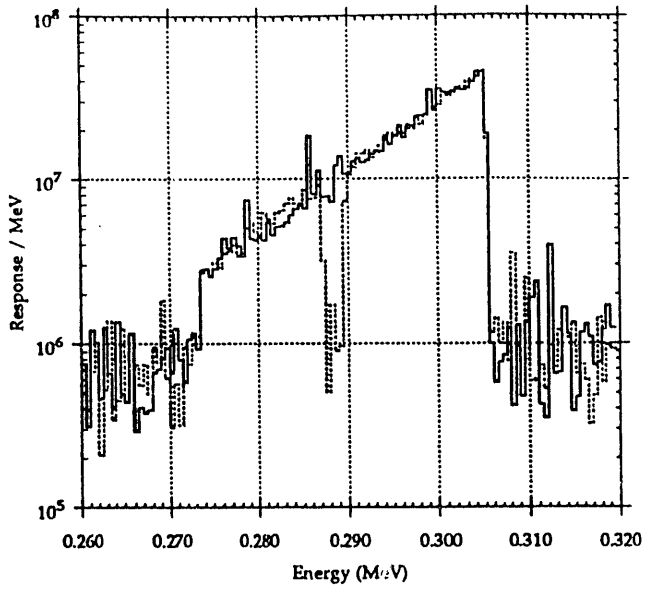

Figure 8b - COG spectrum for an iron target with a 2 mm void filled with iron at 80% nominal density (solid line) compared to the baseline iron spectrum with an air-filled void (dashed line).

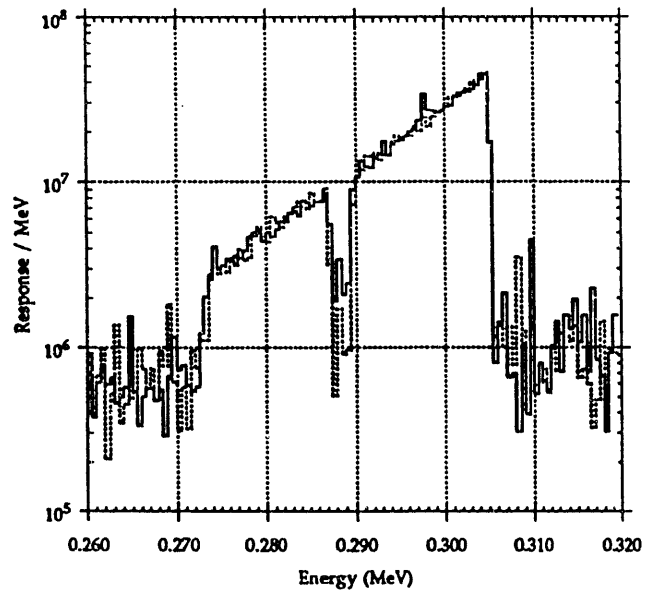

Figure 8c - COG spectrum for an iron target with a 2 mm void filled with cocaine-HCl at 0.90 g/cc (solid line) compared to the baseline iron spectrum with an air-filled void (dashed line).

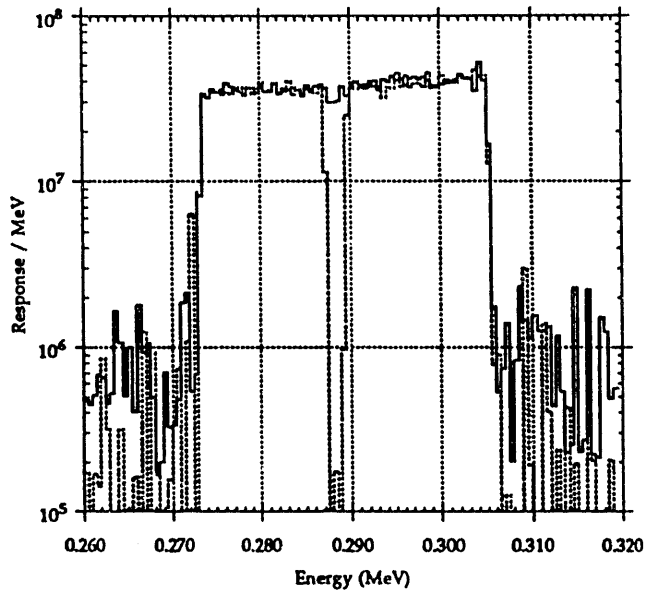

Figure 8d - COG spectrum for a wood target with a 2 mm void filled with cocaine-HCl at 0.90 g/cc (solid line) compared to the baseline wood spectrum with an air-filled void (dashed line).

DATE

FILMED

12/6/93

END